

Topology of Superfluid Turbulence: Computing the Alexander Polynomial

Robert G. Cooper



MMath Dissertation
Academic Year 2016/17
Supervised by Prof. Carlo Barenghi



Abstract

We seek to determine the topological complexity of a small patch of turbulence in superfluid helium away from solid or periodic boundaries. Since superfluids have quantised vorticity we observe the formation of tangled filamentary structures which evolve over time. With the aid of the knot invariant known as the Alexander polynomial, we show that at any time step our tangle consists of mostly *unknots* and vortex knots of low complexity but that there always exist some loops of high geometrical and topological complexity. We then go on to compare the topological complexity with the geometry and dynamics of the system finding a clear increase in complexity with relation to geometrical properties such as length and writhe.

Contributions

Numerical simulations of superfluid turbulence were produced by A.W. Baggaley and M. Mezgarnezhad. A.W. Baggaley's code also calculated all geometrical properties such as length and energy over time. All numerical computations relating to the Alexander polynomial and the writhe were written, developed and tested from scratch by the author. The 3D boxed tangle graphics with shadows were produced by the author building an extension to previous code also written by M. Mezgarnezhad.

Contents

1	Filamentary Structures in Nature	5
2	Introduction to Knot Theory	7
2.1	Projections and Crossings	8
2.2	Writhe	8
2.3	Knot Equivalence and Knot Invariants	9
2.3.1	The Reidemeister Moves	9
2.3.2	Knot Polynomials and Invariants	9
3	Computing the Alexander Polynomial	12
3.1	Examples	13
3.2	Testing	14
4	Knotting in Superfluids	18
4.1	Properties of Quantum Vorticity in Superfluids	18
4.2	Numerical Simulation of Superfluid Vortices	19
4.3	Simulating Turbulence	19
4.4	Topological Complexity	24
5	Conclusions	32

Chapter 1

Filamentary Structures in Nature

There are many occurrences in nature of tangled or disordered filamentary structures ranging from the geodynamo model of the Earth's geomagnetic field [1] to nematic liquid crystals found in neurofilaments [2]. It is often of interest to know whether such structures are in fact knotted and how complicated they are, for example knots in DNA filaments can provide valuable information on the global arrangement of DNA molecules [3]. DNA finds it easier to replicate itself when it is less knotted and thus it is useful to know about the complexity of DNA such that enzymes can be produced which unknot complex strands [4].

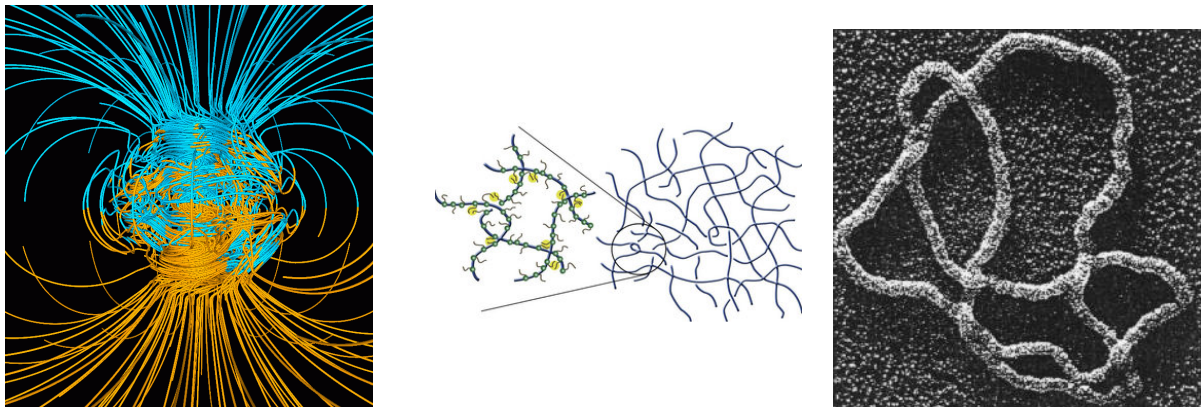


Figure 1.1: (a): The geodynamo simulated with the magnetic field lines indicated as blue and yellow filaments [1]. (b): Nematic liquid crystals in hydrogels of neurofilaments [2]. (c): A three-dimensional closed DNA filament [5].

In this report we are interested in superfluid vortices; superfluid vortices in a patch of turbulence can be visualised and studied through the vortex filament model. Our aim is to study the topological complexity of such vortex filaments and to determine whether they are truly knotted or are in fact trivial *unknots* (circles) in order to relate the topology to the dynamics and geometry of the superfluid.

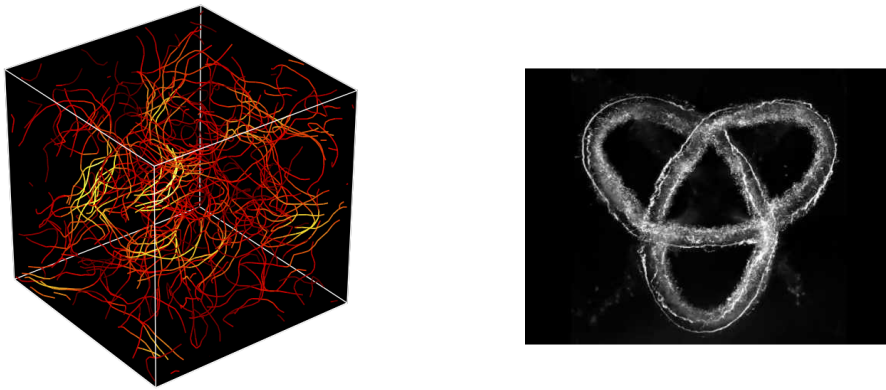


Figure 1.2: (a): A tangle of superfluid vortex filaments simulated in [6]. (b): A knotted vortex filament visualised in water [7].

Chapter 2

Introduction to Knot Theory

Knots are a common phenomena regularly encountered in every day life, whether it be to tie two strings together, or to untangle your headphones in your pocket. They were initially discovered in prehistoric fossils and are common place in the physical world, however knots are also of particular interest in science and nature as mentioned in the previous section. More relevant to us are the mathematical knots found in closed vortex filaments within a region of superfluid turbulence, which knot together forming complex tangles. We are interested in the topology and complexity of such turbulent vortex knots so require methods and properties found in knot theory which will be introduced in this section.

Vandermonde first formed a mathematical theory of knots in 1771, noting the importance of their topology which remains a subject of interest today. The study of knots gained pace in the late 19th century with Gauss, Lord Kelvin and Tait, who produced a table of standard knots. The topology of knots continued to be a subject of fascination into the 20th century with the knot group and topological invariants such as Alexander's polynomial being discovered. Since then significant developments have been made in the field, with a variety of applications ranging from biology to applied mathematics. We will be interested in the knots exhibited in superfluid turbulence and will require multiple results from knot theory to investigate the topology of individual vortex loops simulated numerically by the code of A.W. Baggaley.

Definition 1. (*Knot*) A knot, \mathcal{L} , is a 3D, closed curve which does not intersect itself and can not be simplified without cutting.

We will often be considering complex systems containing many filamentary structures which will often knot with each other as well as with themselves, we define this composition of structures as a tangle.

Definition 2. (*Tangle*) A tangle, \mathcal{T} is a union of two or more knots, \mathcal{L} , which can not be separated from each other without cutting.

When considering the topological complexity of our system of turbulent superfluid vortices we will be focussing on individual loops rather than the full tangle but will be comparing results between tangles at different time steps and under varying drive strengths.

2.1 Projections and Crossings

It is often convenient for us to project knots into a two-dimensional plane in order to consider where the knot crosses below or above itself. This aids in the calculation of many properties of knots such as linking, writhing and helicity however many properties are dependent on the chosen projection. Fortunately numerical experiments in [8] suggest that many properties only require a small number of projections to determine average values which is convenient considering the computational power required to calculate such properties of extremely complex knots.

In order to display knots on paper we must project them into a two-dimensional plane. The section of the knot passing below another will be indicated by a break in the line. Additionally, knots can be oriented to include a direction of travel around the curve thus each crossing can be assigned a numerical representation dependent on the directions of the under passing and over passing segments of the curve according to Figure 2.1. Such crossing numbers, $\epsilon_k = \pm 1$, are particularly useful when calculating properties of a knot or tangle such as the writhing number or linking number as aforementioned.

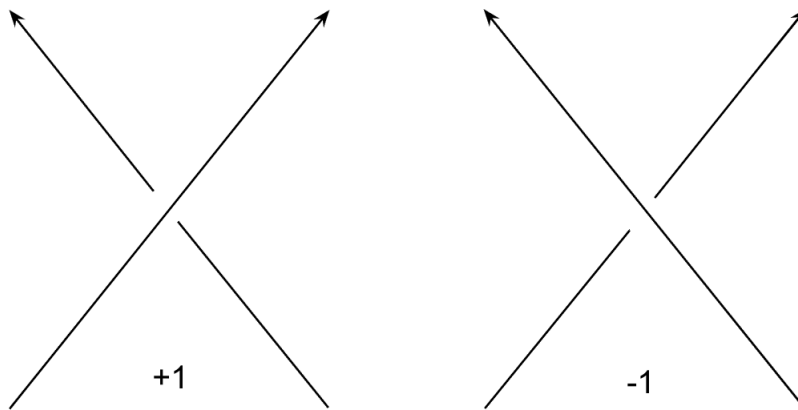


Figure 2.1: The standard notation of crossing directions

Previously, simply counting the number of crossings, usually averaged over a number of projections, was considered as a suitable measure of complexity [9]. However this ignores the possibility of a knot appearing to be more complicated than it actually is. For example if a simple knot is greatly deformed, then the crossing number may be high even though it is a relatively simple knot. In order to truly consider the topological complexity we must find a way of identifying multiple knots as being the same, however this is no easy task.

2.2 Writhe

The writhe is a property of knots which sums numerical values assigned to each apparent crossing, giving an overall measure of the geometry of the configuration. We project a knot,

\mathcal{L} into a two-dimensional plane and find all of the crossings, labelling the crossing numbers according to Figure 2.1, we then sum the crossing number over all of the crossings giving the writhe in a particular projection. Since the writhe varies depending on the two-dimensional projection chosen, taking multiple projections and averaging gives a good estimate of the overall writhe. We will average over the three Cartesian projections since computation over only a small number of projections suffices according to numerical experiments [8]. The writhe of a knot, \mathcal{L} is thus:

$$Wr(\mathcal{L}) = \langle \sum_j \epsilon_j \rangle \quad (2.1)$$

where $\langle \dots \rangle$ denotes the average over the three Cartesian projections.

2.3 Knot Equivalence and Knot Invariants

We wish to be able to determine whether two knots are in fact different diagrams/projections of the same knot or whether one can be deformed into the other. More formally, we wish to know if the two knots are equivalent.

Definition 3. (*Equivalence*) Two knots, \mathcal{L}_1 and \mathcal{L}_2 , are equivalent if there exists a homeomorphism $h : \mathbb{R}^3 \rightarrow \mathbb{R}^3$ with $h(\mathcal{L}_1) = \mathcal{L}_2$.

Unfortunately it is very difficult to tell whether two knots are in fact equivalent due to the lack of existence of a unique way of classifying knots and their properties. We can transform a knot into another knot using the Reidemeister moves which will be explained in the following subsection and attempt to show that two knots are equivalent this way, however this would take some time for more complicated knots.

2.3.1 The Reidemeister Moves

The Reidemeister moves are a set of moves discovered by Reidemeister in 1927, which can be performed to manipulate a knot with the intention of either simplifying it or showing that it is equivalent to another knot, preserving the overall topology of the knot. The moves themselves are displayed in Figure 2.2 and involve twisting or untwisting a segment or moving a segment across another segment or a crossing. We will later use the Reidemeister moves as a means of testing the accuracy of the numerical computations performed. Since they preserve the topology we can perform any of the three moves on our simulated filamentary structures and re-computation of invariant properties should return the same values.

2.3.2 Knot Polynomials and Invariants

A knot invariant is a property that remains the same between equivalent knots, thus multiple projections and diagrams of the same knot will give identical values of such invariants. We will be particularly interested in knot polynomials which are polynomials

whose coefficients represent some of the properties of a knot. If two knots have differing knot polynomials then the two knots are not equivalent, unfortunately the reverse does not hold. Having the same knot polynomial does not necessarily imply that the two knots are the same, for example the 5_1 knot and 10_{132} knot both share knot polynomials yet they are not equivalent.

In 1923 Alexander discovered the first knot polynomial in history. He considered a knot \mathcal{L} , assuming that it was made up of a finite series of straight lines between discrete points (similarly to our data which form vortex loops from straight line segments between pairs of discretised points) and then proposed that \mathcal{L} was topologically equivalent to a simplification of the knot, \mathcal{L}' . He then projected \mathcal{L} and \mathcal{L}' into a plane giving \mathcal{L}_π and \mathcal{L}'_π respectively before considering crossings between pairs of points, adding extra points if there were multiple crossings along the same segment between two points. Alexander then continued to make transformations removing crossings until he had transformed \mathcal{L}_π into \mathcal{L}'_π . [10]. A few years later Alexander published the Alexander polynomial which was dependent on the properties of the knot [11].

Definition 4. (*Alexander Polynomial*) *The Alexander polynomial, $\Delta(\tau)$, is a knot invariant which consists of a polynomial of integer coefficients where the coefficients and order of the polynomial are related to the properties of the knot.*

We will use the Alexander polynomial to analyse the dense tangles of vortices found in a region of superfluid turbulence and their topology. The Alexander polynomial is a typically favoured topological invariant in other research which can easily be coded thanks to the simplicity and multitude of algorithms available. Unfortunately, as previously mentioned the Alexander polynomial cannot completely distinguish all knots, as is the problem with all other knot invariants as some knots share the same polynomial. For example, the trivial *unknot* has Alexander polynomial $\Delta(\tau) = 1$, as does a knot containing 11 crossings in [12]. Although the Alexander polynomial can distinguish between prime knots such as those famously produced and tabulated by Tait. Additionally, the Alexander polynomial can vary by a factor of $\pm\tau^n$ where n is the number of apparent crossings, either for different diagrams of the same knot or depending on the choices made during calculation, thus in order to easily compare two or more knots we require a 'normal' form whereby the initial polynomial calculated is divided through by some power of $\pm\tau$ such that the lowest order element is a positive constant [13].

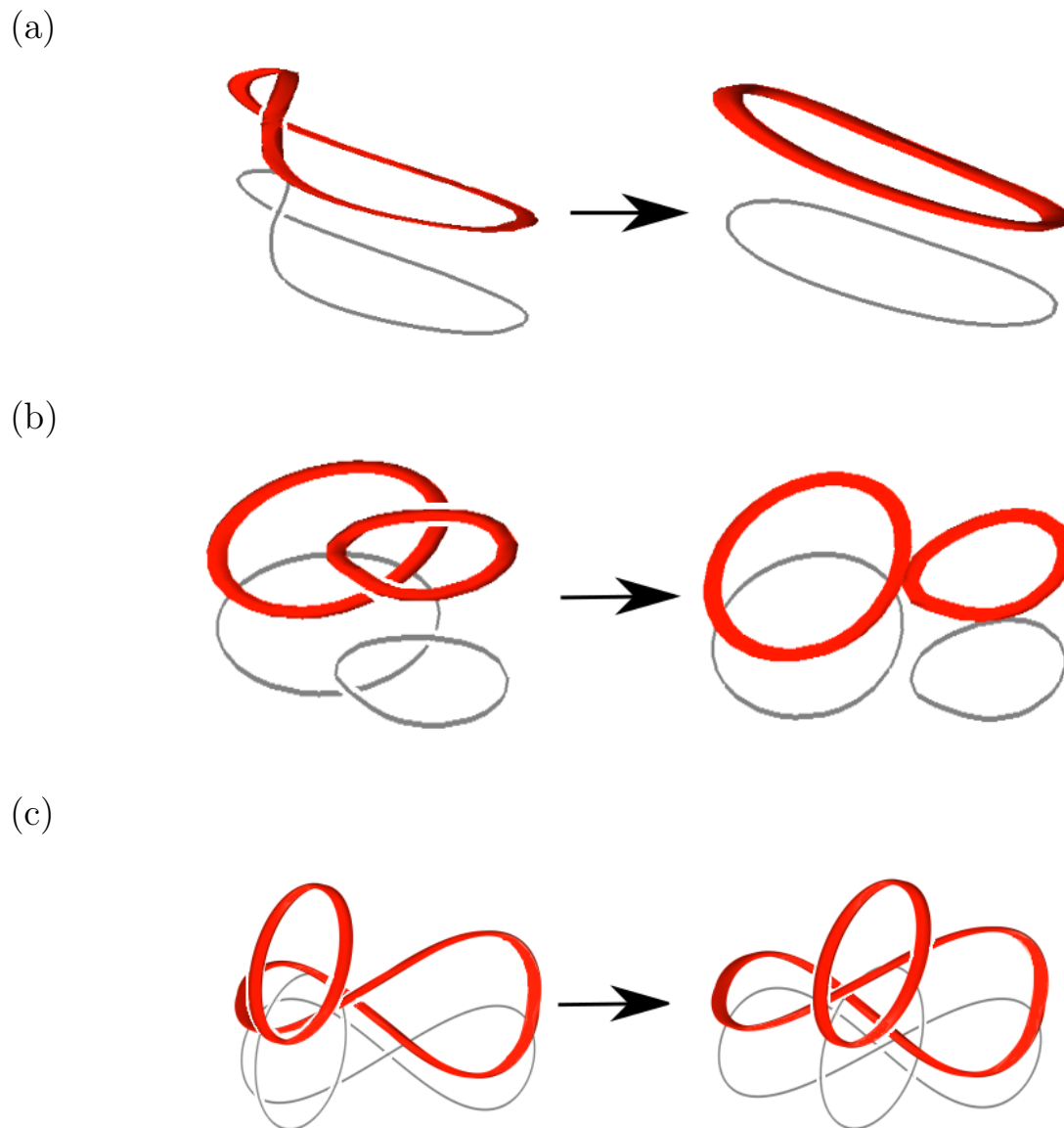


Figure 2.2: The three Reidemeister moves visualised with three dimensional filaments including a shadow projected into the xy -plane. The moves are as follows: (a): The first Reidemeister move which involves twisting or untwisting a loop. (b): The second Reidemeister move involving sliding a loop across another. (c): The third Reidemeister move whereby a loop can be moved over or under a crossing.

Chapter 3

Computing the Alexander Polynomial

There are multiple algorithms which compute the Alexander polynomial however many algorithms involve splitting the knots and reattaching them in different ways which involves an element of human choice and is computationally difficult to code, thus we will use an algorithm defined in [14] which is as follows:

Algorithm 1. (*Alexander Polynomial Algorithm*)

- (1) Project the loop into an arbitrary 2D plane.
- (2) Starting from any point, label the segment it lies on x_1 and follow the knot.
- (3) Each time you pass underneath in a crossing, change the labelling of the line from x_i to x_{i+1} for $i = 1, \dots, n$ where n is the number of crossings.
- (4) Repeat until you return to the original starting point with $x_{n+1} = x_1$.
- (5) Then follow the knot again from the start point, when you pass above a crossing, label that crossing c_1 .
- (6) Repeat as before for c_2, c_3, \dots, c_n .
- (7) Now for each crossing in order, consider the 4 lines that intersect; labelled x_i to x_i above (note that we have not iterated the labelling since this segment passes above in the crossing) and x_j to x_{j+1} below. Beginning from the line exiting over the crossing and moving clockwise, assign coefficients $(1, \tau, -\tau, -1)$ to the relevant x_i 's (see Figure 3.1).
- (8) Now create the matrix, M , of coefficients where the rows correspond to the crossings c_k and the columns correspond to the coefficients of each x_i summing coefficients in the same entry.
- (9) Now delete any 1 column and any 1 row of M forming the matrix M' before taking the determinant giving a polynomial in τ .
- (10) Finally multiply or divide by powers of τ as necessary such that the lowest order power of τ is a positive constant, this is then the Alexander polynomial, $\Delta(\tau)$.

It should be noted that many sources use t as the parameter in the Alexander polynomial, however we will use τ to prevent confusion with t representing time in later Chapters. We will also later define ν as being the order of the Alexander polynomial and use it to

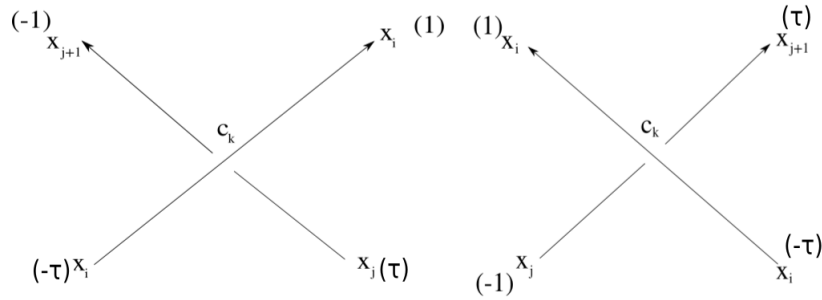


Figure 3.1: Assigning coefficients to overcrossings. (left) When creating the matrix M for a crossing, c_k , with crossing number $\epsilon_k = +1$, in the k th row we write $1 - \tau$ in the i th column (since 2 of the edges are labelled x_i), τ in the j th column, -1 in the $(j + 1)$ th column and zeros elsewhere. (right) If the crossing number is $\epsilon_k = -1$ then we have $1 - \tau$ in the i th column, τ in the $(j + 1)$ th column and -1 in the j th column. Note: if multiple edges have the same index then input the sum of the coefficients.

quantify topological complexity, previously $|\Delta(-1)|$ was often used for such purposes as it can successfully distinguish between many of the standard knots tabulated by Tait and so we will define $\chi = |\Delta(-1)|$ and compare this measure with the order of the Alexander polynomial, ν . We will use subscripts to denote a single individual loop for example ν_j and will drop subscripts for the total over the whole tangle.

3.1 Examples

In the Appendices, three examples are considered. Firstly we compute the Alexander polynomial of the basic 3_1 knot more commonly known as the *trefoil*, which has an Alexander polynomial of $\Delta(\tau) = 1 - \tau + \tau^2$, next we distort the *trefoil* in Example 2 by means of the first Reidemeister move, twisting two of the side segments. As expected its Alexander polynomial is equal to that of Example 1. Finally we consider the 4_1 knot (often called the *figure-eight* knot) which has an Alexander polynomial of $\Delta(\tau) = 1 - 3\tau + \tau^2$. The results of these three examples are consistent with their true Alexander polynomials, which can be found in [11].

Since the Alexander polynomial is a knot invariant, any distortion of the *trefoil* by means of Reidemeister moves will also have the same polynomial of $1 - \tau + \tau^2$ as seen in Example 2. Thus if we find the Alexander polynomial for a given knot and it happens to be the same as that of the basic *trefoil* then it is possible that we may be able to transform and simplify our knot into the *trefoil*. However this is not necessarily always true. The Alexander polynomial is not unique, thus two knots having the same polynomial does not necessarily imply that they are equivalent knots, only that they could be and this is a large limitation of using the Alexander polynomial to attempt to identify knots.

Some examples of standard knots and their Alexander polynomials can be found in

Table 3.1, as well as some examples from our numerical simulations which will be further explained in Chapter 4. The first knot is the trivial *unknot* which has Alexander polynomial $\Delta_j(\tau) = 1$ so has order $\nu_j = 0$ and $\chi_j = 1$, then we have three of the knots tabulated by Tait; the 3_1 (*trefoil*) knot, 5_1 (*Solomon's seal*) knot and the 6_2 knot named the *Miller Institute Knot*. Just from looking at the images we can see an increase in complexity, as seen in the increasing magnitudes of χ_j and ν_j . The right hand column of Table 3.1 contains six vortex loops taken from our numerical simulations of superfluid vortices. The first vortex loop has $\chi_j = 1$ and $\nu_j = 0$ just like an unknot, and this loop can in fact be deformed into the trivial *unknot* at the top of the left hand column. If we had calculated $\chi_j = |\Delta_j(-1)|$ for the next vortex loop we would find $\chi_j = 0$ and may infer that this is also an *unknot*, however its Alexander polynomial is of order $\nu_j = 8$ and so it is not an *unknot*. The remaining four vortex loops in particular highlight how ν_j seems to be a better measure of topological complexity than $\chi_j = |\Delta_j(-1)|$. Visually we can perceive an increase in complexity as we look at the loops going downwards, which is reinforced by ν_j . However χ_j fluctuates largely and so may not be as good a method of quantifying topological complexity.

In Figure 3.2 we attempt to increase topological complexity by combining a mixture of standard and numerically simulated loops. When the Alexander polynomial is then computed it is the product of the Alexander polynomials for each of the loops before attaching. So for example, the first case involves combining two *trefoils*, each with Alexander polynomial $\Delta(\tau) = 1 - \tau + \tau^2$, for the newly formed loop the Alexander polynomial is $\Delta(\tau) = (1 - \tau + \tau^2)^2$, the same holds for combining three *trefoils* and so on. However this result is not unique only to the *trefoil*; Figure 3.2(c) combines the 4_1 knot with the 5_2 knot resulting in an Alexander polynomial which is the product of their original polynomials and Figure 3.2(d) takes a numerically simulated vortex loop with an Alexander polynomial of order $\nu_j = 6$ and attaches it to a mirror image of itself, resulting in an Alexander polynomial of order 12 which is the product of the two polynomials before combining.

3.2 Testing

In Algorithm 1, we are required to project a loop into a 2D plane in order to find crossings, since the Alexander polynomial is a topological invariant the resulting polynomial calculated should be independent of the projection chosen, even though the number of crossings will vary with the projection. In order to test our numerical calculation of the Alexander polynomial we can project the vortex loop into different planes. After projecting into the *xy*-plane, *yz*-plane and *zx*-plane as seen in Figure 3.3, the algorithm programmed computes the same Alexander polynomial of order 202 as expected.

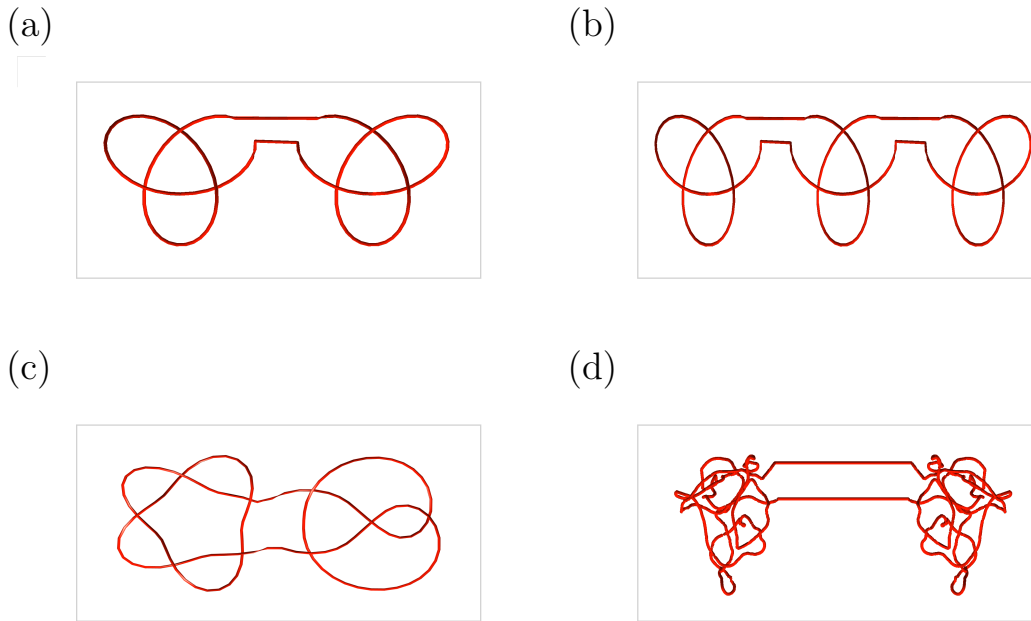


Figure 3.2: Combining both standard and numerically simulated loops we see that the Alexander polynomial of the resulting loop is the product of the Alexander polynomials for each component. For example, (a): Combining two *trefoils* with Alexander polynomial $\Delta(\tau) = 1 - \tau + \tau^2$ gives a loop of polynomial $\Delta(\tau) = (1 - \tau + \tau^2)^2$. (b): The same applies to three *trefoils* giving an Alexander polynomial of order $\nu_j = 6$ and $\chi_j = |\Delta_j(-1)| = 9$. (c) This holds for knots other than *trefoils* too, here we combine a 4_1 (*figure-eight*) knot with a 5_1 (*Solomon's Seal*) knot, each with Alexander polynomials of orders 2 and 4 respectively and both with $\chi_j = 5$. The result is a knot whose Alexander polynomial is the product of the polynomials of the 4_1 knot and 5_1 knot which is of order $\nu_j = 6$ and has $\chi_j = 25$. (d): Here we combine a numerically simulated knot with a mirror image of itself. The knot has an Alexander polynomial of order $\nu_j = 6$ with $\chi_j = 11$ and after combining, the Alexander polynomial is of order $\nu_j = 12$ with $\chi_j = 121$.

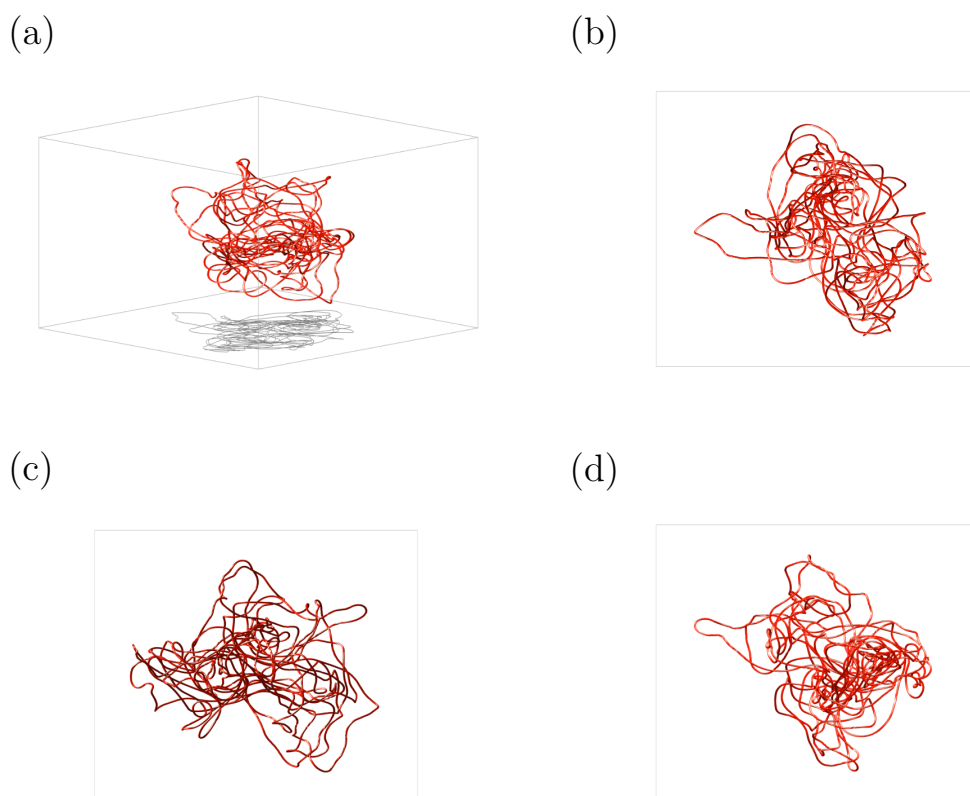


Figure 3.3: (a): A knotted filamentary structure which we compute as having a lengthy Alexander polynomial of order $\nu_j = 202$ with $\chi_j = 215197$ when projected into the following three different planes, (b): the xy -plane, (c): the yz -plane, and (d): the xz -plane.













Knot	χ_j	ν_j	Knot	χ_j	ν_j
	1	0		1	0
	3	2		1	8
	5	4		15	46
	11	4		9747	82
	17	4		381	108
	15	4		15871481	232

Table 3.1: A table of a selection of standard and numerically simulated knots with their Alexander polynomials evaluated at $\tau = -1$, χ_j and their orders, ν_j . The left hand column contains six standard knots; the *unknot*, 3_1 (*trefoil*) knot, 5_1 (*Solomon's Seal*) knot, 6_2 (*Miller Institute*) knot, 7_5 knot and 8_{21} knot. In general both ν and $\chi = |\Delta(-1)|$ increase, with the order increasing at a slower rate. The first knot in the right hand column has an Alexander polynomial of order $\nu_j = 0$ so may be an *unknot* and in fact can easily be manipulated by hand into the *unknot*. However the second knot on the right which was numerically simulated also has $\chi_j = 1$, so one may think that this is an *unknot*, yet the order of its Alexander polynomial tells us that it is not. $\chi = |\Delta(-1)|$ is able to distinguish between many of the standard knots tabulated by Tait, however we may require something else for the more topologically complex knots found in our simulations; the order of the Alexander polynomial. The lower four numerically simulated knots highlight the fact that the order of the Alexander polynomial, ν seems to be a more practical and accurate measure of topological complexity, as by eye we can perceive an increase in complexity going downwards coinciding with ν_j but not necessarily χ_j .

Chapter 4

Knotting in Superfluids

As previously mentioned, tangled filamentary structures can be found in superfluid vortices which have a physical interpretation in the form of quantum superfluids (such as ^4He and ^3He) and atomic Bose-Einstein condensates. Vortices lose energy by undergoing reconnection events where two vortices approach each other then reconnect changing the topology of the flow. The methods used for simulating superfluid vortices will be outlined below, however they are also available in [15].

4.1 Properties of Quantum Vorticity in Superfluids

Two important properties of superfluids are that they have zero viscosity and quantised circulation. The former property makes them similar to Euler fluids and the latter property stems from the existence of a complex macroscopic wavefunction $\Psi(\mathbf{x}, t) = \sqrt{n(\mathbf{x}, t)}e^{i\phi(\mathbf{x}, t)}$ where \mathbf{x} is position, t is time and $n(\mathbf{x}, t)$ is the number density in accordance with the Madelung approximation [16]. The superfluid velocity is then proportional to the gradient of the phase, that is:

$$\mathbf{v}(\mathbf{x}, t) = \frac{\hbar}{m}\nabla\phi \quad (4.1)$$

where m is the mass of the relevant boson and \hbar is the reduced Planck's constant $\hbar = h/(2\pi)$ with $h = 6.63 \times 10^{-34}\text{Js}$. As Ψ is single-valued the circulation of the velocity field of the superfluid around C , which is a closed path, can either be zero or a multiple of the quantum circulation $\kappa = h/m$:

$$\oint_C \mathbf{v} \cdot d\mathbf{r} = n\kappa \quad (4.2)$$

for $n = 0, \pm 1, \pm 2, \dots$. The path C encloses a vortex line when $\Psi \neq 0$, in this project we will only be concerned with the case where $n = \pm 1$. The axis of the vortex line has a thin core region of radius $a_0 \approx 10^{-10}\text{m}$ in ^4He where the number density $n(\mathbf{x}, t)$ becomes zero making vortex lines holes with quantised superfluid circulation surrounding them.

4.2 Numerical Simulation of Superfluid Vortices

Previous numerical simulations of the Gross-Pitaevskii equation which governs Ψ have shown that vortex reconnections occur when vortices come within a few core lengths of each other [17], and in the process of reconnecting some of their kinetic energy is released in the form of density waves [18]. Vortex reconnections are of great importance in the dynamics of a turbulent superfluid.

Typically the average separation between vortices is many orders of magnitude larger than the radius of the vortex core a_0 thus we can model superfluid vortices as closed curves in space $\mathbf{s}(\xi, t)$ where ξ is the arc-length and the curves are infinitesimally thin. Below 1K liquid helium acts as a pure superfluid whose vortices move according to [19]:

$$\frac{d\mathbf{s}}{dt} = \mathbf{v}_{self}(\mathbf{s}) \quad (4.3)$$

where \mathbf{v}_{self} is self-induced velocity given by the Biot-Savart integral:

$$\mathbf{v}_{self}(\mathbf{s}) = -\frac{\kappa}{4\pi} \oint_{\mathcal{L}} \frac{(\mathbf{s} - \mathbf{r}) \times d\mathbf{r}}{|\mathbf{s} - \mathbf{r}|^3} \quad (4.4)$$

over a vortex configuration \mathcal{L} . The superfluid vortex lines are simulated numerically using a Lagrangian discretisation of the lines [20] which have a variable number of discrete points as more points are required in areas of higher curvature. The Biot-Savart integral in Equation (4.4) is de-singularised as in [20] and a procedure for vortex reconnections is implemented algebraically [21].

However, we are concerned with temperatures above 1K in which thermal excitations form a normal fluid which unlike the superfluid does have viscosity and has a velocity field denoted \mathbf{v}_n . The superfluid part and the normal fluid part transfer energy by a mutual friction force [22] which requires a modification to Equation (4.3) [20]:

$$\frac{d\mathbf{s}}{dt} = \mathbf{v}_{self} + \alpha \mathbf{s}' \times (\mathbf{v}_n - \mathbf{v}_{self}) - \alpha' \mathbf{s}' \times [\mathbf{s}' \times (\mathbf{v}_n - \mathbf{v}_{self})] \quad (4.5)$$

where α and α' are small coefficients dependent on the temperature due to interactions between the vortex lines and the thermal excitations in the normal fluid.

4.3 Simulating Turbulence

We wish to numerically simulate a patch of superfluid turbulence where we reach a statistically steady state independently of the arbitrary initial condition and are away from solid or periodic boundaries so that the superfluid vortex lines generated are closed. Turbulence away from boundaries has been achieved experimentally using ultrasound waves to create vortices [23]. Here the vortex lines decay as they leave the central region due to friction with the normal fluid which is stationary away from the centre region as seen

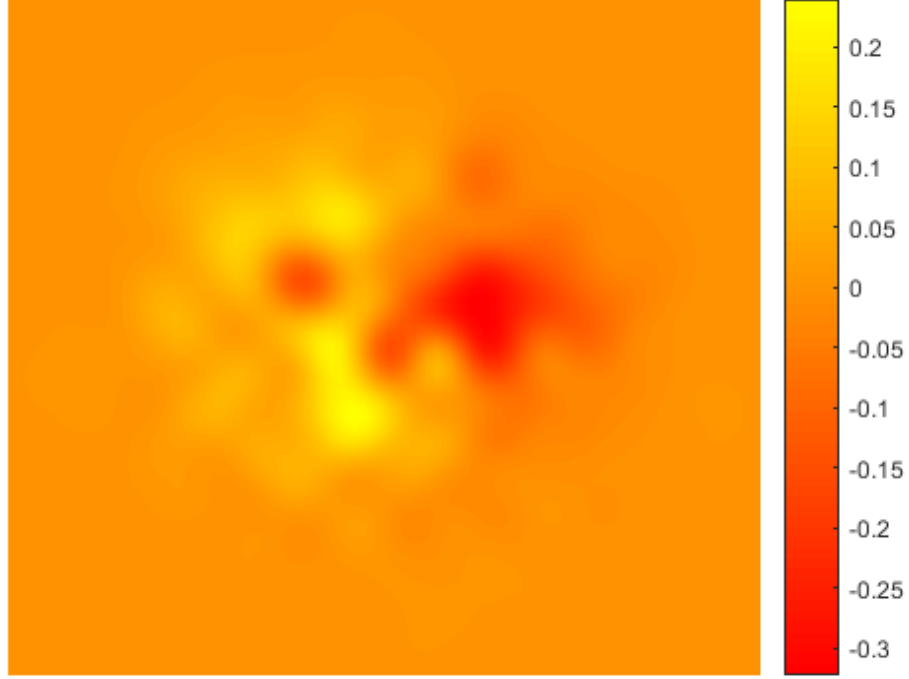


Figure 4.1: The magnitude of the driving normal fluid velocity \mathbf{v}_n in cm s^{-1} taken at an arbitrary time with $-2.5 \leq x \leq 2.5$, $-2.5 \leq y \leq 2.5$, $z = 0$.

in Figure 4.1. To model this we impose a normal fluid velocity field consisting of the Arnold-Beltrami-Childress flow (ABC flow) multiplied by an exponential decay.

The ABC flow is an exact solution of the Euler equation defined by velocity components:

$$\mathbf{v}_A(x, y, z, t) = \begin{pmatrix} B \cos(ky - \omega t) + C \sin(kz - \omega t) \\ C \cos(kz - \omega t) + A \sin(kx - \omega t) \\ A \cos(kx - \omega t) + B \sin(ky - \omega t) \end{pmatrix} \quad (4.6)$$

where A , B and C are constants, k is 8π divided by the size of the region which is $d = 1.5\text{cm}$ and ω is the normal fluid frequency which we set to 1. The normal fluid velocity, \mathbf{v}_n is then determined by applying an exponential decay to the velocity of the ABC flow:

$$\mathbf{v}_n(x, y, z, t) = \mathbf{v}_A(x, y, z, t) e^{-\sqrt{x^2+y^2+z^2}/d} \quad (4.7)$$

Previously we had chosen our velocity field to consist of random waves in the centre of the region which decay exponentially outwards [15], however on this occasion the ABC flow was chosen due to the fact that we can easily vary the driving parameters in order to compare the topological complexity to physical properties such as the energy and drive

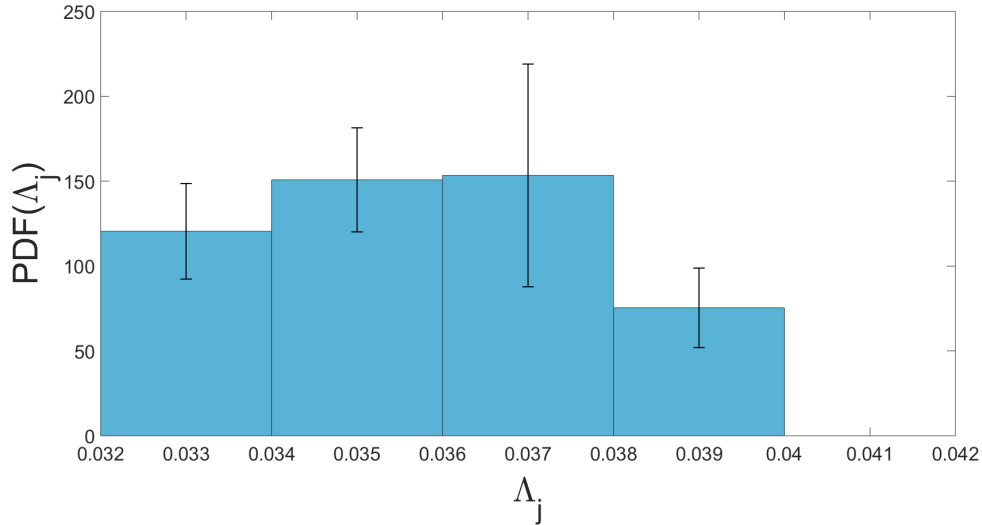


Figure 4.2: The probability density function of the lengths of the initial vortex loops Λ_j in cm over all drives.

velocity of the flow as well as the geometry of the turbulence. It is also advantageous that the ABC flow has vorticity parallel to the velocity as we thus only need to drive the fluid more intensely to increase the vorticity. All simulations are performed at a temperature of 1.9K which is typical of experiments and corresponds to $\alpha = 0.206$ and $\alpha' = 8.43 \times 10^{-3}$ and we use an initial condition of 40 randomly oriented loops with sizes varying according to a normal distribution with an average number of 200 points, located at the centre of the region. The probability density function of the initial loop lengths can be seen in Figure 4.2. We set $A = B = C$ and compare how varying the drive parameter affects the energy, length and topological complexity and if there is any relationship between these measures.

We observe that the initial vortex configuration expands in length due to instability with the tightly packed vortices reconnecting and releasing Kelvin waves. The overall topology of the system is continuously altered by the regular reconnections and the tangle quickly reaches a statistically steady turbulent state. An example of the tangle evolution is seen in Figure 4.3 with a drive of $A = 1$. In Figure 4.4 we see that the total length, Λ of the vortices in a tangle at each time step initially increases before fluctuating around an average value as we reach a statistically steady state and Figure 4.5 shows that the majority of vortices remain small at each time step and for all drives. We do however find at least some much larger vortex loops. Increasing the drive parameters in the ABC flow results in longer turbulent vortex tangles.

The energy is calculated by [19]:

$$E = \rho \int_V \mathbf{v} \cdot \mathbf{r} \times \boldsymbol{\omega} dV \quad (4.8)$$

where V is the volume and ρ is the density which we set to unity as the fluids simulated are incompressible. Assuming that $\mathbf{v} \rightarrow 0$ at infinity and using the fact that the vorticity

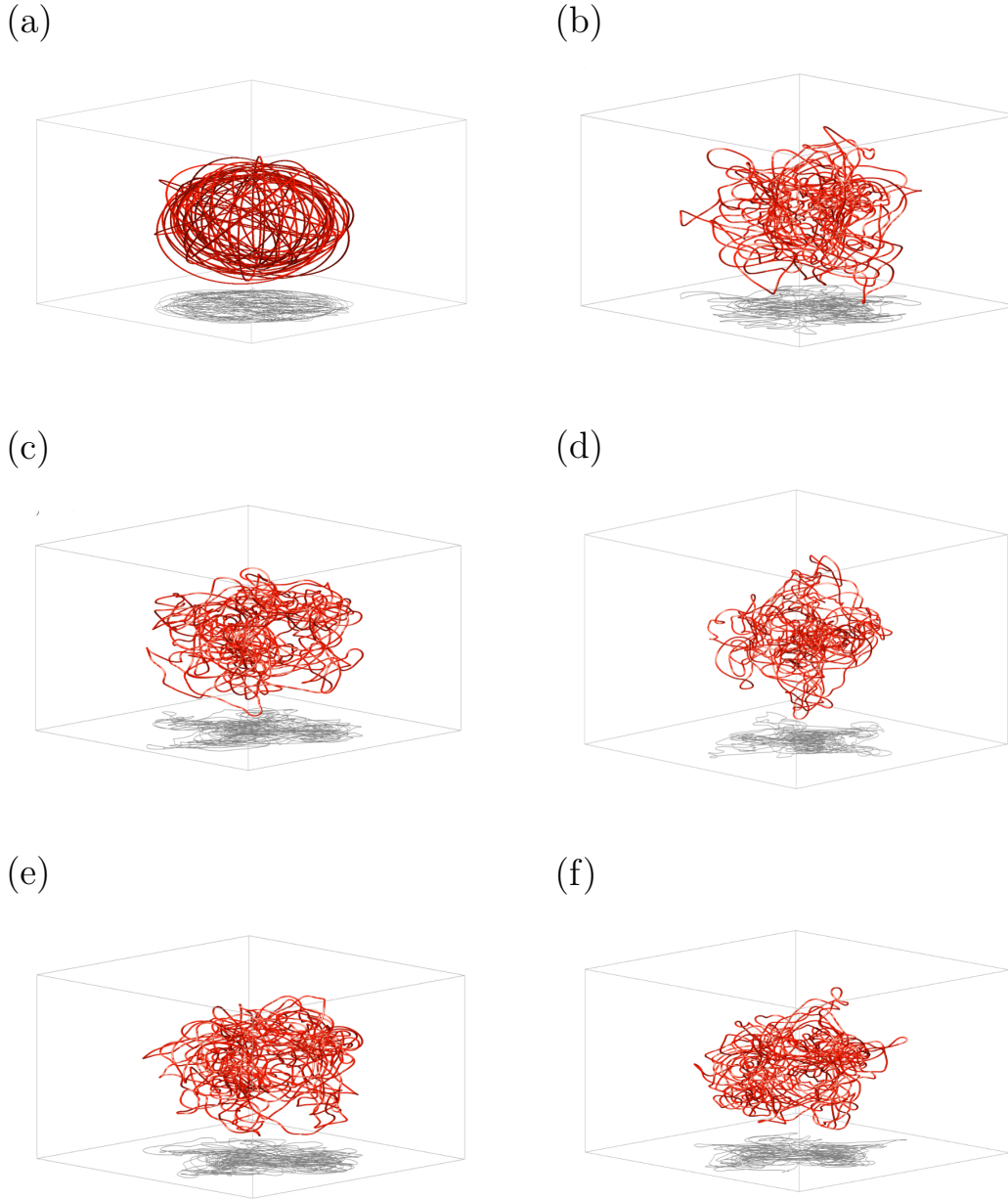


Figure 4.3: The typical time evolution of the vortex tangle with a drive of $A = 1$. The vortex lines are the red curves, equally scaled and enclosed in a box with shadows for visualisation purposes only. The figure shows the vortex tangle at (a): The initial condition, $t = 0.00s$ in the region $-0.50 \leq x \leq 0.40$, $-0.45 \leq y \leq 0.45$, $-0.45 \leq z \leq 0.45$. (b): $t = 0.20s$ in the region $-3.10 \leq x \leq 2.75$, $-3.10 \leq y \leq 2.75$, $-3.1 \leq z \leq 2.75$. (c): $t = 1.96s$ in the region $-3.10 \leq x \leq 2.75$, $-3.10 \leq y \leq 2.75$, $-3.10 \leq z \leq 2.75$. (d): $t = 6.00s$ in the region $-3.50 \leq x \leq 3.60$, $-3.70 \leq y \leq 3.40$, $-3.60 \leq z \leq 3.60$. (e): $t = 13.92s$ in the region $-3.20 \leq x \leq 2.60$, $-3.00 \leq y \leq 3.20$, $-3.20 \leq z \leq 2.60$. (f): $t = 26.08s$ in the region $-3.20 \leq x \leq 3.00$, $-2.90 \leq y \leq 3.20$, $-3.00 \leq z \leq 3.20$.

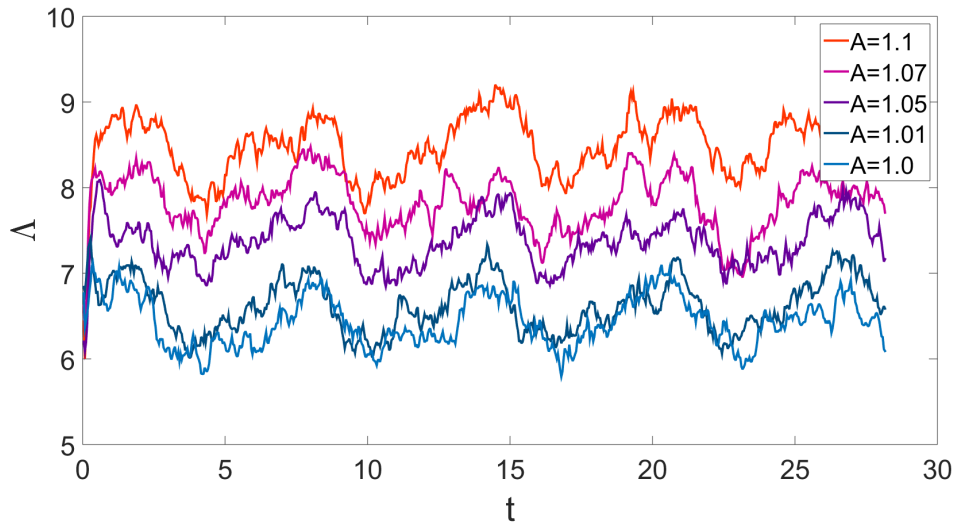


Figure 4.4: Tangle length, Λ in cm vs time, t in s. The tangle length rapidly increases at early times before fluctuating around an average value for all drives with an increased drive resulting in a larger tangle length.

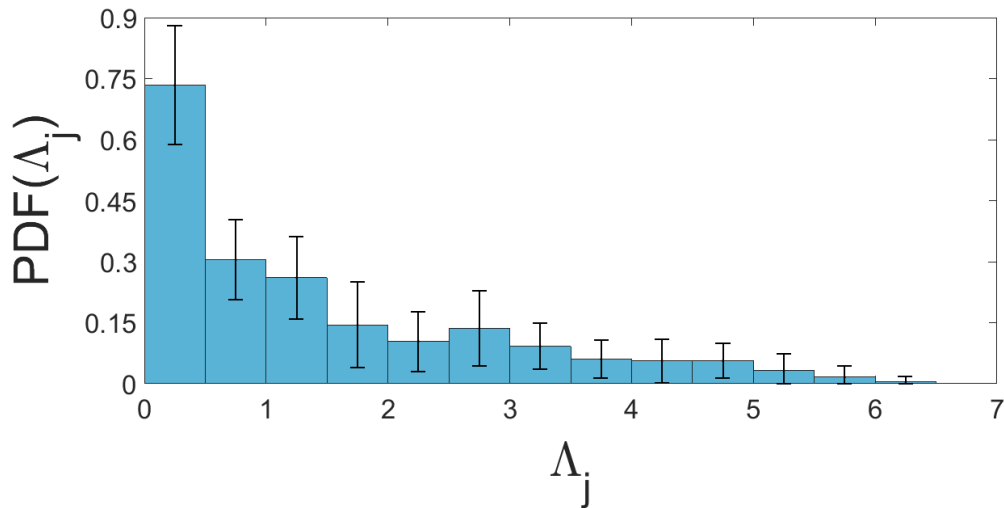


Figure 4.5: The probability density function of the length of individual vortex loops, Λ_j in cm over all drives. We see a decay in the frequency of vortices with length indicating that at each time step and for each drive we see many small vortex loops and very few large loops.

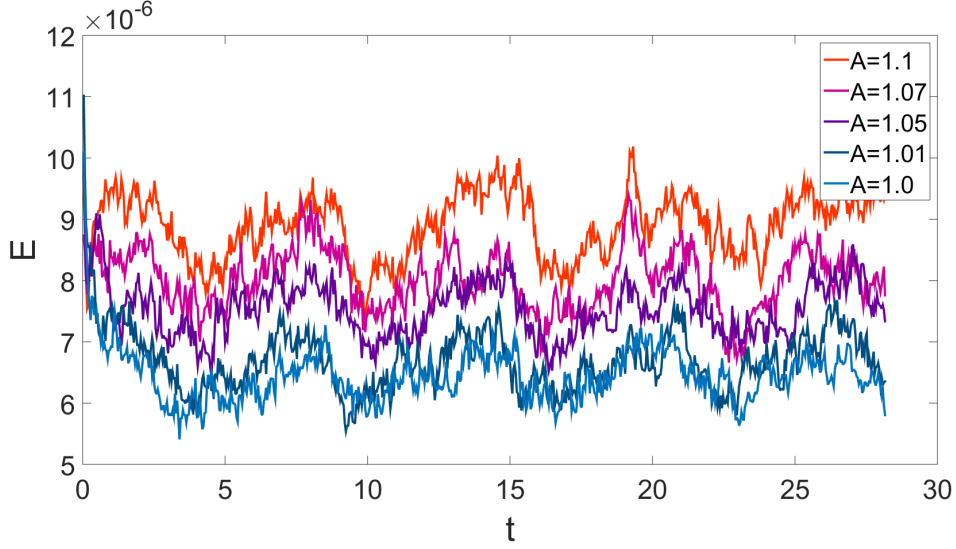


Figure 4.6: Kinetic energy, E of the vortex configuration in arbitrary units vs time, t in s. The energy quickly decays before settling down and fluctuating around an average value which is higher for higher drives.

is concentrated to the filaments themselves we have:

$$E = \kappa \oint_{\mathcal{T}} \mathbf{v} \cdot \mathbf{r} \times \mathbf{s}' d\xi \quad (4.9)$$

where the integral is over the whole vortex tangle \mathcal{T} with tangent vector \mathbf{s}' and arc-length ξ . In Figure 4.6 we observe that energy instantly decreases before fluctuating around an average value with higher drives resulting in higher energies.

4.4 Topological Complexity

In previous research, evaluating the Alexander polynomial of a given loop at $\tau = -1$ is used to quantify topological complexity such as in [24]. This is due to the fact that $|\Delta(-1)|$ can distinguish and classify many of the standard knots with low topological complexity. However, many of the superfluid vortices we numerically simulate are much more complex and so we will use the order of the Alexander polynomial, ν in an attempt to better quantify topological complexity, comparing with $|\Delta(-1)|$ throughout. We therefore define topological complexity of a vortex loop in two different ways, using the order of the Alexander polynomial for a loop j , ν_j and $\chi_j = |\Delta(-1)|$. So for example, a loop with polynomial

$$\Delta_j(\tau) = a_0 + a_1\tau + \dots + a_{\nu_j}\tau^{\nu_j} \quad (4.10)$$

is of order ν_j and has

$$\chi_j = |\Delta_j(-1)| = |a_0 + a_1(-1) + \dots + a_{\nu_j}(-1)^{\nu_j}| \quad (4.11)$$

We will then compare both the order of the Alexander polynomial and $\chi_j = |\Delta_j(-1)|$ with geometrical properties such as length and writhe as well as the dynamics of the superfluid.

Figure 4.7 shows a selection of simulated vortices with a range of topological complexities as indicated by the order of their Alexander polynomials and $\chi_j = |\Delta_j(-1)|$. In (a) we see a vortex with an Alexander polynomial of order $\nu_j = 0$, which is the same polynomial as that of the trivial *unknot* and can in fact be easily transformed into a basic *unknot*. We see in Figure 4.8 that the majority of vortex loops have Alexander polynomials of order $0 \leq \nu_j \leq 10$ such as those displayed in Figure 4.7 (a)-(c) where we also see a deformed *trefoil* and *Solomon's Seal*, however there always exist vortices of high topological complexity such as those in (d)-(f). These always have a lengthy and complicated Alexander polynomial of high order with an extremely large value of χ_j . The knots of highest complexity at each time reach orders as high as $\nu_j \sim 300$.

When comparing the order of the Alexander polynomial, ν_j against the drive, we see in Figure 4.10 that in general a higher drive does result in vortex loops of higher topological complexity and that they occur more frequently. As is the case for χ_j in Figure 4.11. Often a vortex tangle for a lower drive contains only one vortex of high topological complexity with the remaining vortices being far less topologically complex. However for higher drives we occasionally see for example two or more vortices which reach Alexander polynomials of $\nu \geq 100$ with large values of χ_j . However both ν_j and χ_j largely fluctuate so no strong relationship can be determined. Little relationship was found between topological complexity and energy.

When we compare the topological complexity with the geometry of the system we see in Figures 4.12 and 4.13 that both the order of the Alexander polynomial, ν_j and the value of the polynomial when evaluated at $\tau = -1$ increase with vortex length. In the case of ν_j the order of the Alexander polynomial seems to increase exponentially just as in [15], however there is some scatter for higher lengths and complexities. Additionally, when the logarithm of the order was taken and plotted against length the data were far from linear in contrast to [15]. The logarithm of $\chi_j = |\Delta_j(-1)|$ when plotted against the vortex length Λ_j is closer to linear suggesting a vague linear relationship between the two, however the data do largely vary. Figure 4.14 shows similar probability density function for the writhe to that found with the order of the Alexander polynomial, ν_j and χ_j . In Figure 4.15 we see a striking result in that the order of the Alexander polynomial, ν_j certainly seems to increase linearly with the writhe, successfully relating the topological complexity with the geometry of our vortex filaments. No such relationship seems to exist for χ_j however in Figure 4.16.

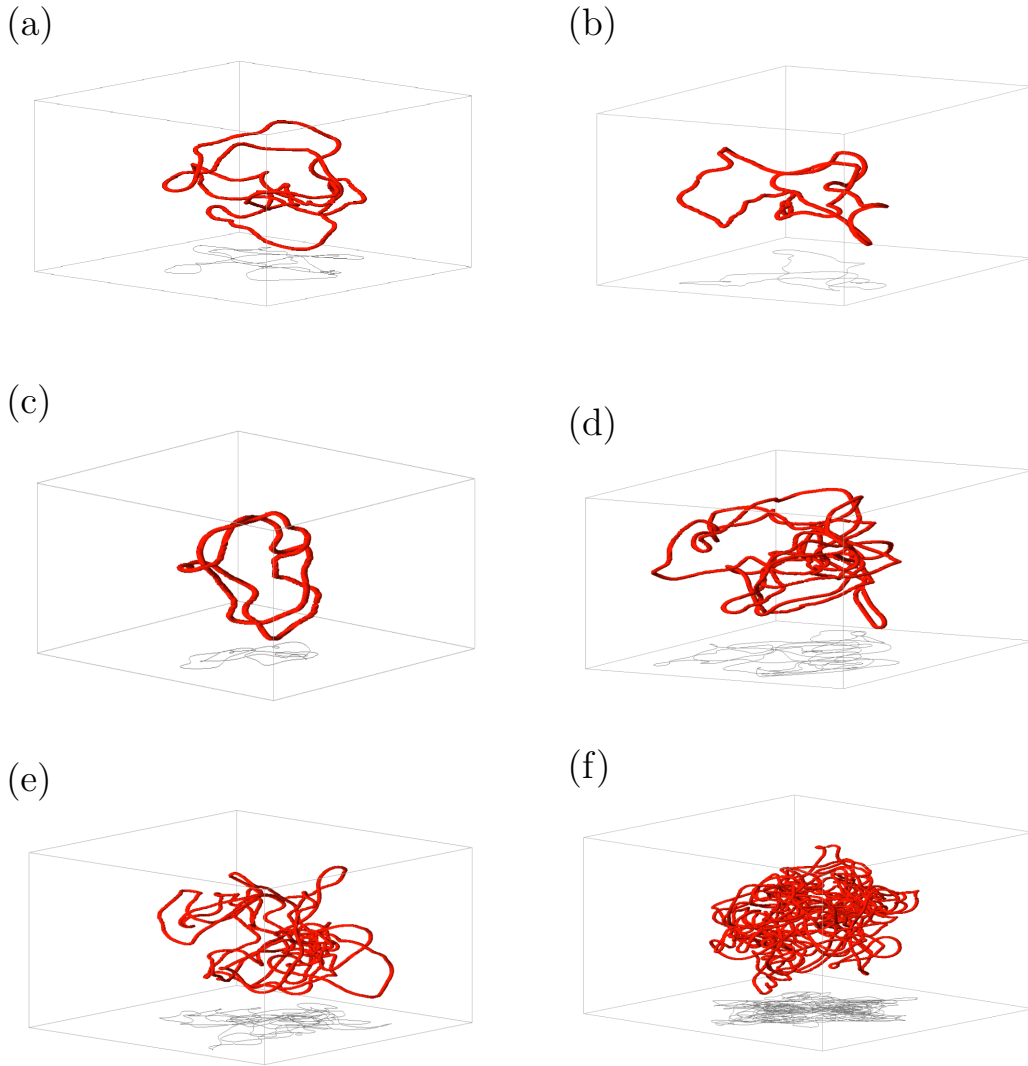


Figure 4.7: Examples of vortex loops with given Alexander polynomial, boxed with shadows in the xy -plane for visual purposes. (a): An *unknot* with Alexander polynomial of order $\nu_j = 0$ and $\chi_j = 1$. (b): This vortex loop has an Alexander polynomial of $\Delta(\tau) = 1 - \tau + \tau^2$, $\nu_j = 2$ and $\chi_j = 3$ and can easily be manipulated into a *trefoil*, which can almost be seen in the xy -projection. (c): A numerically simulated vortex loop with $\Delta(\tau) = 1 - \tau + \tau^2 - \tau^3 + \tau^4$ which is of order 4 with $\chi_j = 5$, this is in fact a *Solomon's Seal*. (d): A slightly more complex loop with an Alexander polynomial of order $\nu_j = 28$ and $\chi_j = 57$. (e): This vortex has an Alexander polynomial of order $\nu_j = 54$ with $\chi_j = 63$. (f): One of the most topologically complex vortices found in our simulations with a polynomial of order $\nu_j = 450$ and $\chi_j \approx 9.6 \times 10^{10}$.

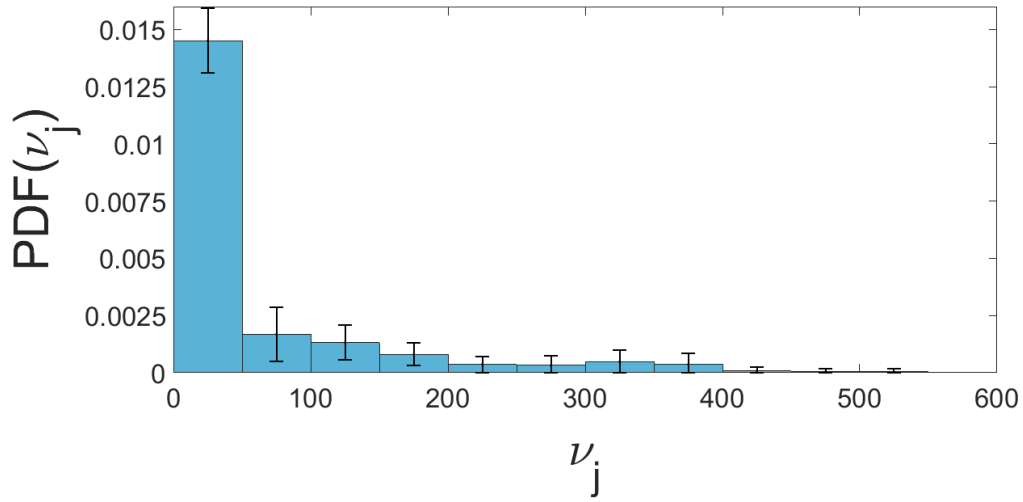


Figure 4.8: The probability density function of the order of the Alexander polynomial, ν_j for individual vortex loops over all drives. For all drives, and at all time steps we see that there are many vortex loops of low topological complexity (such as *unknots* or *trefoils*) with low ordered Alexander polynomials, but that there always exist highly complex vortices with large Alexander polynomials.

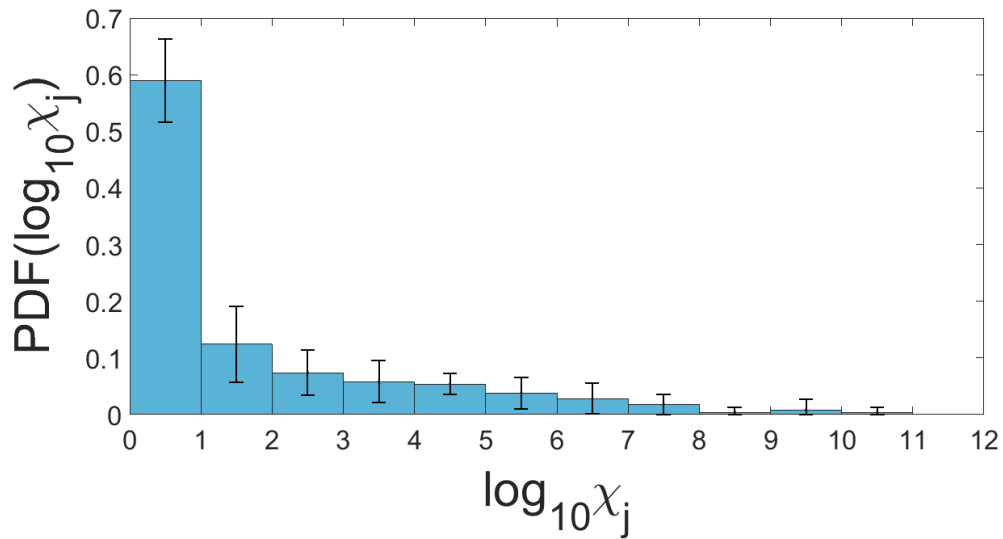


Figure 4.9: The probability density function of $\chi_j = |\Delta_j(-1)|$ over all drives. As with the order of the Alexander polynomial, we see that there are always many vortex loops with lower values of χ_j and at least one vortex of high topological complexity with large values of χ_j .

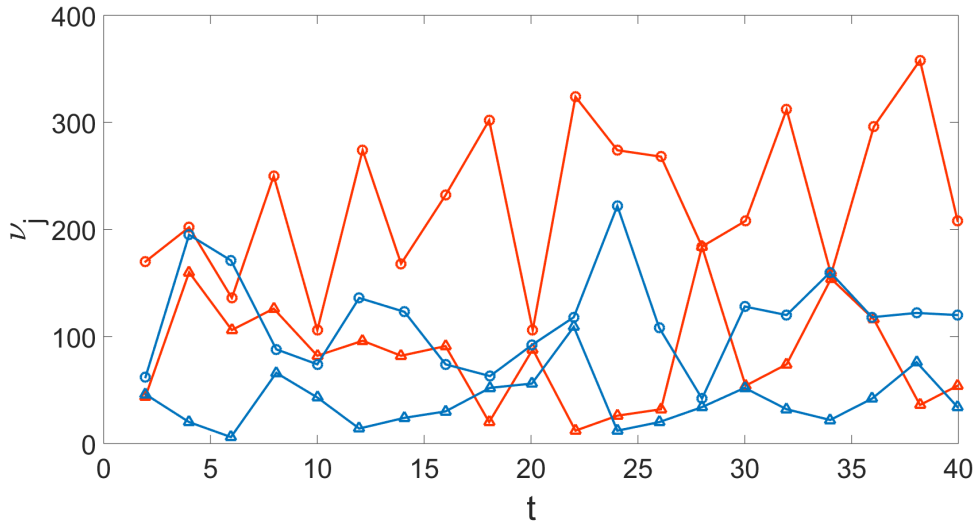


Figure 4.10: The time evolution of the highest and second highest ordered Alexander polynomials, ν_1 (circles) and ν_2 (triangles) respectively for a higher drive of $A = 1.1$ (red) and lower drive of $A = 1.0$ (blue). In general, we see that higher drives tend to results in vortices with a higher ordered Alexander polynomial. However ν_j does greatly fluctuate so we cannot make any strong conclusions.

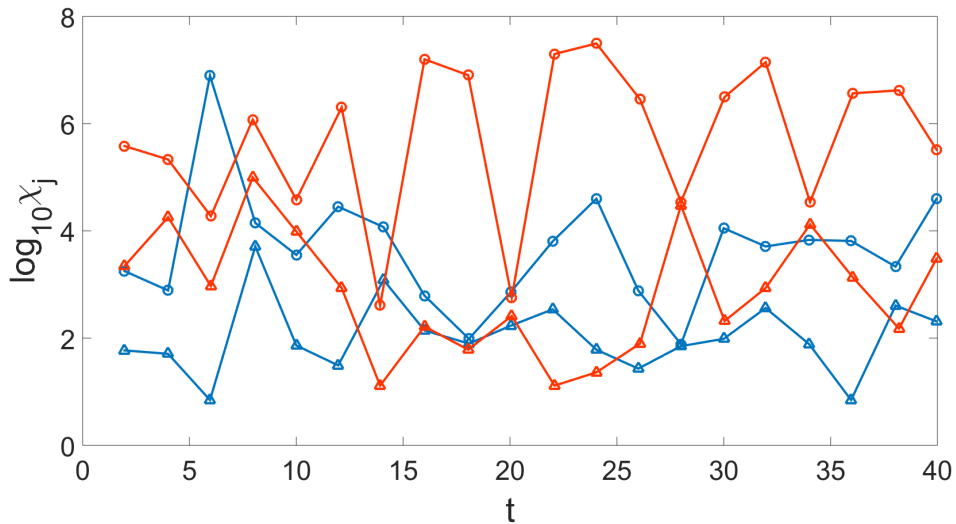


Figure 4.11: The time evolution of the logarithm of the highest and second highest values of $\chi_j = |\Delta_j(-1)|$, χ_1 (circles) and χ_2 (triangles) respectively, for a higher drive of $A = 1.1$ (red) and lower drive of $A = 1.0$ (blue). For the higher drive we see that χ_1 is almost always higher than for the lower drive but that for χ_2 this is not always the case.

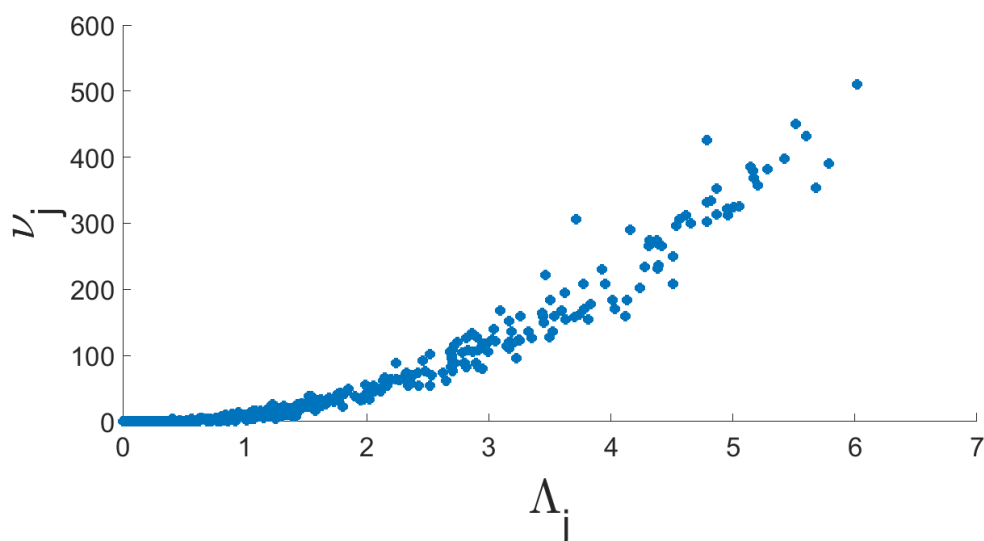


Figure 4.12: The order of the Alexander polynomial, ν_j for each vortex against vortex length, Λ_j in cm. We see that ν_j increases with length and there may be some sort of exponential relationship.

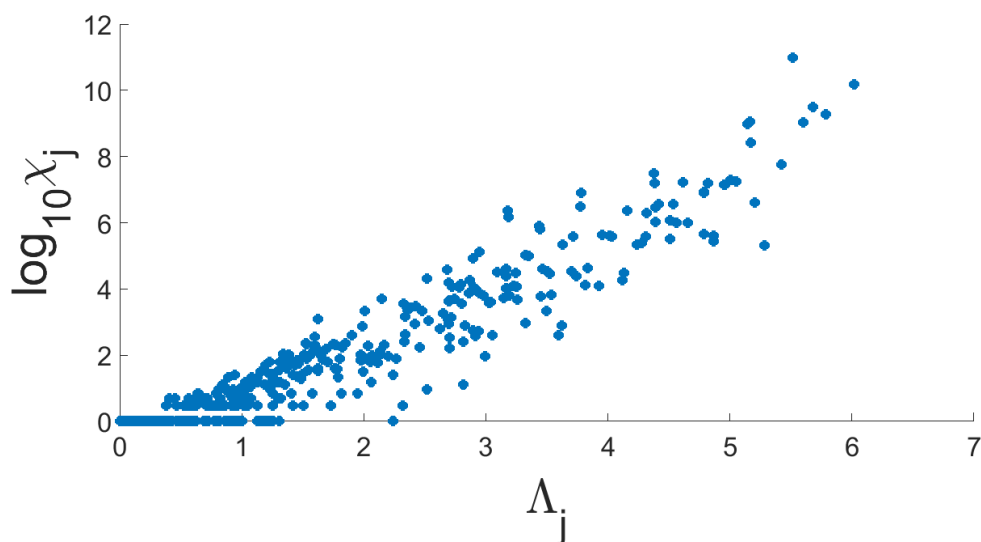


Figure 4.13: The logarithm of $\chi_j = |\Delta_j(-1)|$ versus the vortex length, Λ_j measured in cm. χ_j increases almost linearly with Λ_j however there is a fairly large amount of scatter.

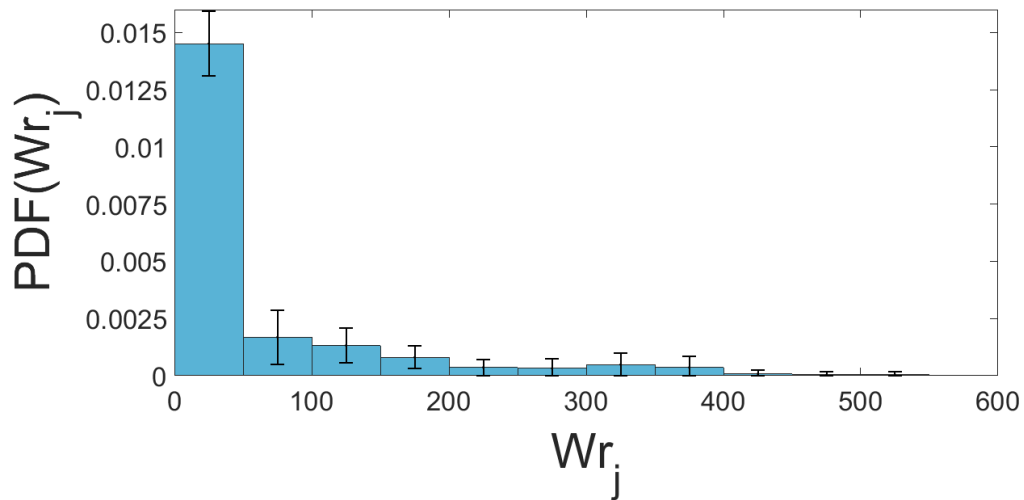


Figure 4.14: The probability density function of the writhe of individual vortex loops, Wr_j over all drives. We see many vortices of low writhe and very few with much larger writhes and geometrical complexity.

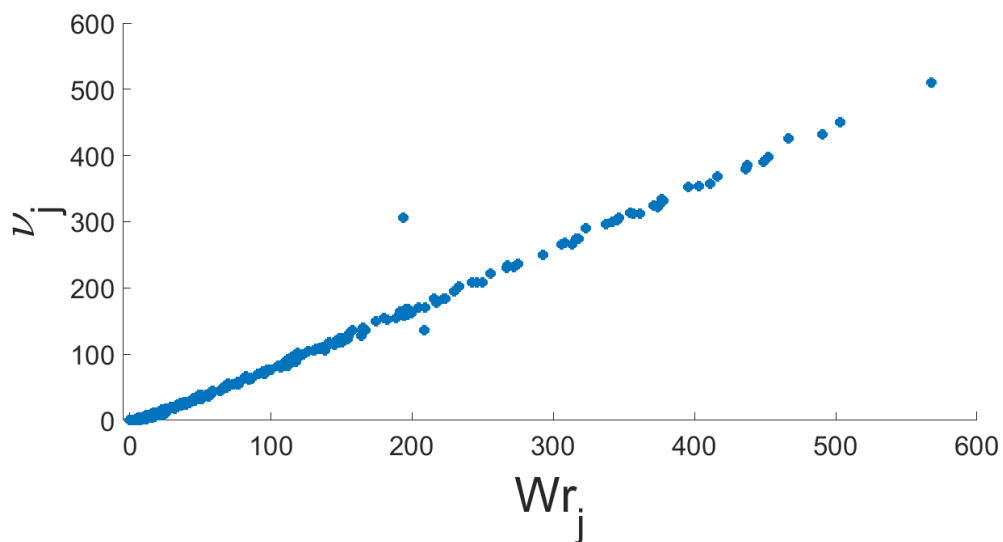


Figure 4.15: Comparing the order of the Alexander polynomial, ν_j with the writhe, Wr_j . Clearly there appears to be a linear relationship between the order of the Alexander polynomial and the writhe of a vortex loop.

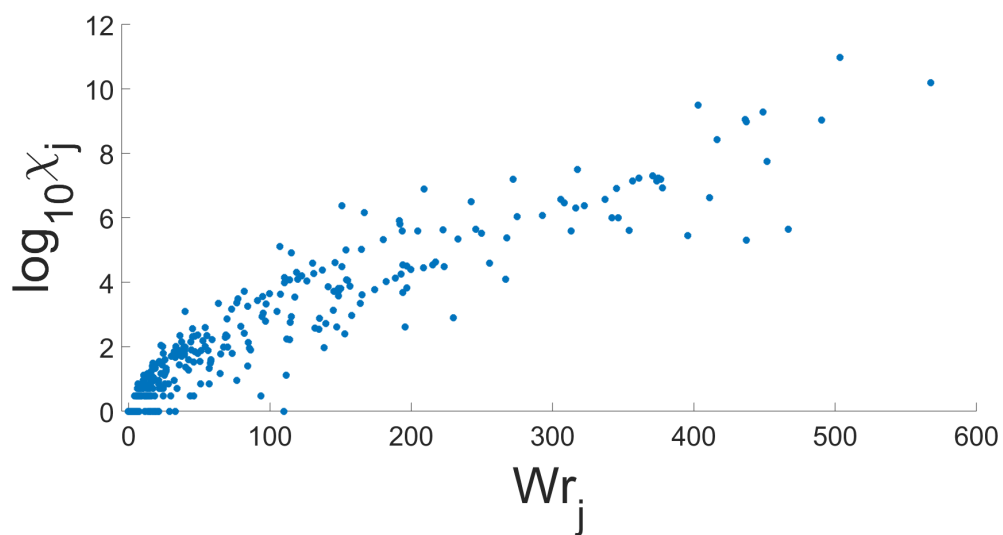


Figure 4.16: The logarithm of the Alexander polynomial evaluated at $\tau = -1$, χ_j versus the writhe, Wr_j of each vortex loop. In general, the logarithm of χ_j increases with Wr_j however the rate of increase appears to be slowing.

Chapter 5

Conclusions

In this report we numerically simulate a patch of superfluid turbulence which reaches a statistically steady state away from solid or periodic boundaries. We then quantify the topological complexity of superfluid vortices through the knot invariant known as the Alexander polynomial and compare the complexity with the geometry and dynamics of the turbulent patch of superfluid. Little research has previously been performed in the absence of solid or periodic boundaries so we will mostly compare results with our previous paper where we drive the normal fluid using random waves placed at the centre of the domain which decay exponentially outwards [15].

In Chapter 3 we outline one algorithm which computes a knot invariant known as the Alexander polynomial. We then show examples of how the order of the Alexander polynomial successfully quantifies topological complexity along with its evaluation at $\tau = -1$. The combining of two knots or vortex loops generally results in a more complex Alexander polynomial of higher order thus demonstrating the adequacy of the order of the Alexander polynomial, ν_j as a measure of topological complexity. Previously $\chi_j = |\Delta_j(-1)|$ was often used to quantify topological complexity and we provide evidence that this is suitable for vortex loops of low complexity but that the order of the Alexander polynomial is arguably better for the more complex configurations of vortex filaments found in our numerical simulations.

We find that at each time step and for each drive velocity our vortex tangles consist mostly of vortices with low topological complexity but that there always exist some vortices of extremely high topological complexity with large Alexander polynomials. This is in agreement with the results found for a different normal fluid drive velocity consisting of random waves with an initial condition consisting of equally sized vortex rings in [15]. We however, find a much lower number of vortices at each time than when using random waves and we also discover vortex loops of much higher complexity as indicated by the order of their Alexander polynomials and the evaluation of the polynomials at $\tau = -1$ which was not included for the random waves case.

We also compare the topological complexity of the superfluid vortices with geometrical properties such as the length and writhe, as well as the dynamics through the varying drive parameters of the ABC flow.

Unfortunately, although we find a general relationship between topological complexity and the drive of the normal fluid, we still do not know exactly how complexity scales with the drive parameters. Exploring a wider range of drives for the normal fluid ABC flow may help us to better determine a relationship, alternatively we could try other normal fluid flows and consider other measures which define topological complexity.

Comparing the length of a vortex loop with both the order of its Alexander polynomial, ν_j and the value when the Alexander polynomial is evaluated at $\tau = -1$, χ_j we see that the topological complexity increases as the vortex length increases. This is unsurprising as our longest vortices tend to be those which are very dense and look more complicated by eye. The order of the Alexander polynomial seems to increase roughly exponentially with length which is not overly dissimilar to DNA molecules when modelled as random polygons, where the probability of a polygon being an *unknot* (thus having low topological complexity) decreases exponentially with length [24]. [25] also found that the probability of a polymer configuration being knotted increased with length. However, unlike in [15], when the logarithm of ν_j was plotted against length there was little evidence of linearity suggesting that this may not entirely be the case. In contrast a strong linear correlation was found between the writhe of a vortex loop and the order of its Alexander polynomial which directly relates topological complexity with the geometry of the superfluid vortices.

In further work it would be interesting to consider other natural systems which contain filamentary structures, for example magnetic fields and other continuous cases in contrast to our discretised superfluid vortices. This however presents a new problem; to compute the Alexander polynomial and other topological properties of knots we require our filamentary structures to be closed. We must find a method of closing any filamentary structures which terminate at a boundary, such as those shown in Figure 5.1, in order to compute their topological complexity. We briefly attempted to take a turbulent field of a classical fluid in a periodic box and form closed vortex lines but struggled and abandoned the idea, however if such a method could be discovered it would enable us to compare the topological complexity between superfluids and classical fluids, as well as other continuous systems.

Repetition of the current research with differing initial conditions would also be beneficial to confirm that the vortices of high topological complexity do not occur because of the compactness and close proximity of the initial randomly oriented vortex rings.

Finally, other knot invariants do exist such as the HOMFLY polynomial which actually generalises the Alexander polynomial and another topological invariant known as the Jones polynomial. The HOMFLY is a polynomial of two variables where evaluating the HOMFLY at particular values directly produces the Alexander polynomial. An algorithm for computing the HOMFLY polynomial is outlined in [26] and before deciding on the Alexander polynomial we were able to successfully compute the polynomials for a selection of standard knots such as the *unknot* and *trefoil* by hand, however the algorithm involved changing the orientation of crossings and splitting knots as far as multiple *unknots* which would both be difficult to code and have high computational complexity.



Figure 5.1: A tangle of superfluid vortices in a box [27]. Many of the vortex lines terminate at a boundary, if we could develop a method of closing them we could then calculate the Alexander polynomial and other properties of knots.

Appendices

Example 1. Consider the trefoil in Figure 1. Beginning at a point on the line x_1 , follow

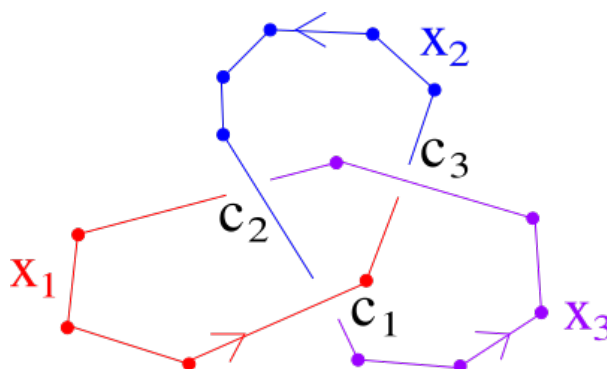


Figure 1: The basic *trefoil*. We have assigned each curve x_i , iterating i each time we pass below in a crossing, followed by assigning each crossing, c_j in order as we pass above in a crossing.

the knot iterating the label after each under pass for x_2 and x_3 , then beginning from the same point each time there is an overcrossing label it c_1, c_2, c_3 .

Now consider each of the crossings in order, assign the relevant coefficients, $(1, \tau, -\tau, -1)$ (Figure 2). After assigning the coefficients we can now form the matrix, M .

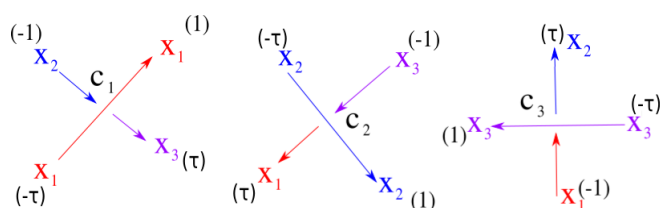


Figure 2: Assigning coefficients (in brackets) to each of the crossings in Example 1.

$$M = \begin{pmatrix} 1 - \tau & -1 & \tau \\ \tau & 1 - \tau & -1 \\ -1 & \tau & 1 - \tau \end{pmatrix}$$

We may now delete any 1 row and any 1 column to form M' , say we delete row 3 and column 2. Then we have:

$$M' = \begin{pmatrix} 1 - \tau & \tau \\ \tau & -1 \end{pmatrix}$$

Taking the determinant of M' :

$$\det(M') = -1 + \tau - \tau^2$$

Since the lowest order power of τ is not a positive constant, we will normalise by dividing through by -1 :

$$\Delta(\tau) = 1 - \tau + \tau^2$$

And this is the Alexander polynomial of the basic trefoil, consistent with the coefficients quoted in [11].

Example 2. Consider the knot in Figure 3 which is in fact a trefoil, only we have twisted two of the sides using the 1st Reidemeister Move.

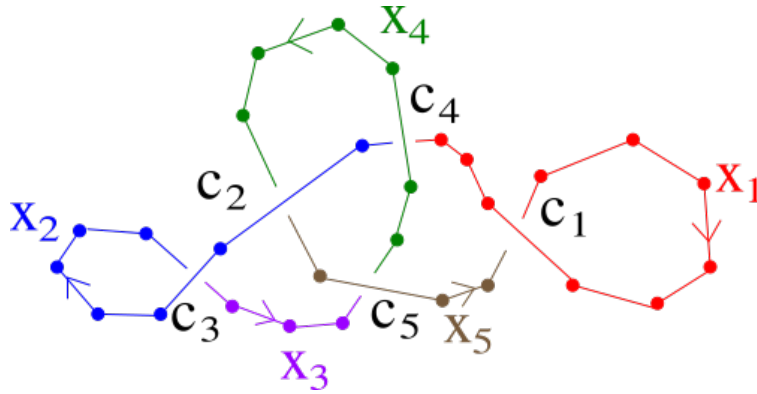


Figure 3: A new knot which is a variation of the *trefoil* seen in Example 1. Again we pass along the knot labelling each curve x_i , which becomes x_{i+1} each time we pass below in a crossing, followed by labelling each crossing c_j as we pass above in a crossing.

Following the same method as before, we start at any point and follow the knot changing the label of the line each time we pass below a crossing. Then we again follow the knot labelling each crossing as we pass over it.

We now consider each crossing in turn and assign the coefficients $(1, \tau, -\tau, -1)$ moving clockwise from the exit of the overpass such as in Figure 4, before collecting the coefficients in the matrix, A .

$$M = \begin{pmatrix} 1 & 0 & 0 & 0 & -1 \\ 0 & 1 - \tau & 0 & \tau & -1 \\ 0 & 1 & -1 & 0 & 0 \\ \tau & -1 & 0 & 1 - \tau & 0 \\ 0 & 0 & \tau & -1 & 1 - \tau \end{pmatrix}$$

We may now delete a single row and column from M , say row 1 and column 4 giving:

$$M' = \begin{pmatrix} 0 & 1 - \tau & 0 & -1 \\ 0 & 1 & -1 & 0 \\ \tau & -1 & 0 & 0 \\ 0 & 0 & \tau & 1 - \tau \end{pmatrix}$$

Now take the determinant of this matrix:

$$\det(M') = -\tau^3 + \tau^2 - \tau$$

And to produce the Alexander polynomial we normalise through dividing by $-\tau$.

$$\Delta(\tau) = 1 - \tau + \tau^2$$

Clearly this is the same Alexander polynomial as we found previously in Example 1

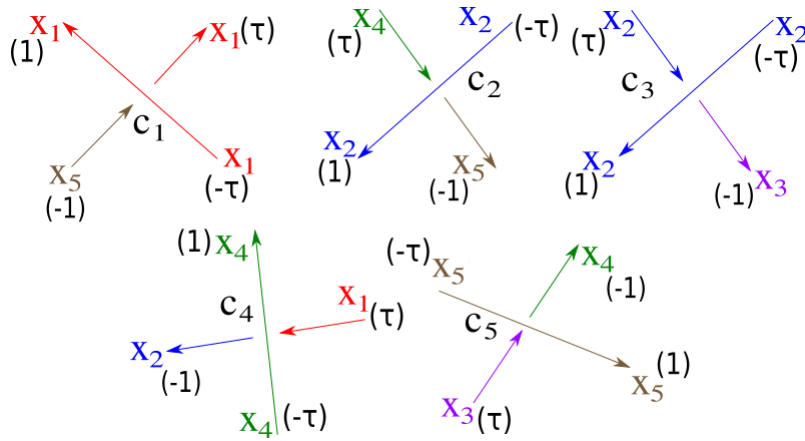


Figure 4: The assigning of coefficients (in brackets) to the *trefoil* variation in Example 2

Example 3. We wish to find the Alexander polynomial of the figure-eight knot in Figure 5, we begin by following the knot labelling the curves x_i , increasing i each time we pass below a crossing. We then label the crossings c_j in the order of which we pass above them.

At each crossing in order we assign the coefficients $(1, \tau, -\tau - 1)$ clockwise from the exit of the overpass (see Figure 6).

And in each row of the matrix, M , we input the relevant coefficients giving:

$$M = \begin{pmatrix} 1 - \tau & -1 & \tau & 0 \\ 0 & 1 - \tau & \tau & -1 \\ \tau & 0 & 1 - \tau & -1 \\ \tau & -1 & 0 & 1 - \tau \end{pmatrix}$$

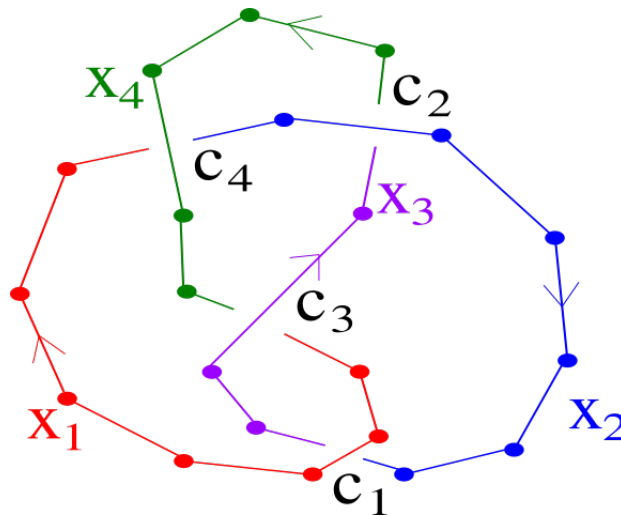


Figure 5: The *figure-eight* knot with curves labelled x_i , and crossings c_j .

We must now decide which row and column to delete, since the choice is arbitrary delete the final row and column which is what the code will be told to do, giving A' :

$$M' = \begin{pmatrix} 1 - \tau & -1 & \tau \\ 0 & 1 - \tau & \tau \\ \tau & 0 & 1 - \tau \end{pmatrix}$$

Now take the determinant of M' .

$$\det(M') = 1 - 3\tau + \tau^2$$

This is already normalised so the Alexander polynomial of the figure-eight knot is

$$\Delta(\tau) = 1 - 3\tau + \tau^2$$

which is the same as recorded in [11].

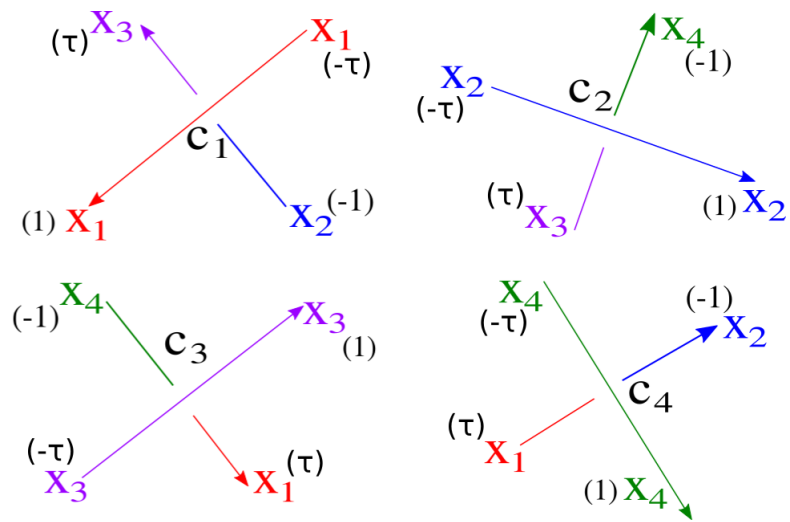


Figure 6: Assigning the coefficients in brackets to each element of the matrix M .

Bibliography

- [1] Glatzmaier G.A. and Roberts P.H. (1995)
A Three-Dimensional Self-Consistent Computer Simulation of a Geomagnetic Field Reversal, *Nature*, **377**, 203
- [2] Deek J., Chung P.J., Kayser J., Bausch A.R. and Safinya C.R. (2013)
Neurofilament Sidearms Modulate Parallel and Crossed-Filament Orientations Inducing Nematic to Isotropic and Re-entrant Birefringent Hydrogels, *Nature Communications*, **4**, 2224
- [3] Arsuaga J., Vazquez M., McGuirk P., Trigueros S., Sumners D.W. and Roca J. (2005)
DNA Knots Reveal a Chiral Organization of DNA in Phage Capsids, *Proceedings of the National Academy of Science USA*, **102**, 9165
- [4] Gross L. (retrieved 21/02/2017)
DNA and Knot Theory, www.tiem.utk.edu/~gross/bioed/webmodules/DNAknot.html
- [5] Sumners D.W. (1990)
Untangling DNA, *The Mathematical Intelligencer*, **3**, 71
- [6] Baggaley A.W., Laurie J. and Barenghi C.F. (2012)
Vortex-Density Fluctuations, Energy Spectra and Vortical Regions in Superfluid Turbulence, *Physical Review Letters*, **109**, 205304
- [7] Kleckner D. and Irvine W.T.M. (2013)
Creation and Dynamics of Knotted Vortices, *Nature Physics*, **9**, 253
- [8] Barenghi C.F., Ricca R.L. and Samuels D.C. (2001)
How Tangled is a Tangle?, *Physica D: Nonlinear Phenomena*, **157**, 197
- [9] Buck G. and Simon J. (1999)
Thickness and Crossing Number of Knots, *Topology and its Applications*, **91**, 245
- [10] Alexander J.W. (1923)
A Lemma on Systems of Knotted Curves, *Proceedings of the National Academy of Sciences*, **9**, 93

- [11] Alexander J.W. (1928)
Topological Invariants of Knots and Links, *Transactions of the American Mathematical Society*, **30**, 275
- [12] Des Cloizeaux J. and Mehta M.L. (1979)
Topological Constraints on Polymer Rings and Critical Indices, *Journal de Physique*, **40**, 7
- [13] Long E. (2005)
Topological Invariants of Knots: Three Routes to the Alexander Polynomial, (Manchester University Thesis)
- [14] Livingstone L. (1993)
Knot Theory, (Cambridge University Press)
- [15] Mezgarnezhad M., Cooper R.G., Baggaley A.W. and Barenghi C.F. (2016)
Helicity and Topology of a Small Region of Quantum Vorticity, *arXiv:1610.10024*
- [16] Barenghi C.F. and Parker N.P. (2016)
A Primer on Quantum Fluids, (Springer)
- [17] Koplik J. and Levine H. (1993)
Vortex Reconnection in Superfluid Helium, *Physical Review Letters*, **71**, 1375
- [18] Zuccher S., Caliarì M., Baggaley A.W. and Barenghi C.F. (2012) Quantum Vortex Reconnections, *Physics of Fluids*, **24**, 125108
- [19] Saffman P.G. (1992)
Vortex Dynamics, (Cambridge University Press)
- [20] Schwarz K.W. (1988)
Three Dimensional Vortex Dynamics in Superfluid ^4He : Homogeneous Superfluid Turbulence, *Physical Review B*, **38**, 2398
- [21] Baggaley A.W. (2012)
The Sensitivity of the Vortex Filament Method to Different Reconnection Models, *Journal of Low Temperature Physics*, **168**, 18
- [22] Barenghi C.F., Donnelly R.J. and Vinen W.F. (1983)
Friction on Quantized Vortices in Helium II. A Review, *Journal of Low Temperature Physics*, **52**, 189
- [23] Schwarz K.W. and Smith C.W. (1981)
Pulsed-Ion Study of Ultrasonically Generated Turbulence in Superfluid ^4He , *Physics Letters A*, **82**, 251

- [24] Arsuaga J., Vazquez M., Trigueros S., Sumners D.W. and Roca J. (2002)
Knotting Probability of DNA Molecules Confined in Restricted Volumes: DNA Knotting in Phage Capsids, *Proceedings of the National Academy of Sciences*, **99**, 5373
- [25] Michels J.P.J. and Wiegel F.W. (1989)
The Distribution of Alexander Polynomials of Knots Confined to a Thin Layer, *Journal of Physics A: Mathematical and General*, **22**, 2393
- [26] Goulding D. (2010)
Knot Theory: The Yang-Baxter Equation, Quantum Groups and Computation of the Homfly Polynomial, (Durham University Thesis)
- [27] Sergeev Y. (2011)
Quantum Turbulence: Energy Dissipation in Extreme Cold, *Nature Physics*, **7**, 451